

# Influence of annealing temperature on the properties of $\text{In}_2\text{S}_3:\text{Sn}$ films deposited by spray pyrolysis

M. Kraini<sup>1</sup> · N. Bouguila<sup>1</sup> · J. El Ghoul<sup>1,2</sup> · I. Halidou<sup>3</sup> · S. A. Gomez-Lopera<sup>4</sup> · C. Vázquez-Vázquez<sup>5</sup> · M. A. López-Quintela<sup>5</sup> · S. Alaya<sup>1,6</sup>

Received: 8 February 2015 / Accepted: 27 April 2015 / Published online: 6 May 2015  
© Springer Science+Business Media New York 2015

**Abstract** Tin-doped  $\text{In}_2\text{S}_3$  films were grown by the chemical spray pyrolysis method using compressed air as a carrier gas. The films were annealed for 2 h at different temperatures (300, 400 and 500 °C) under nitrogen atmosphere. X-ray diffraction data show that  $\text{In}_2\text{S}_3:\text{Sn}$  films are polycrystalline with a cubic phase. The film grain size increases from 26 to 37 nm. The residual microstrain and dislocation network reach the values  $3.08 \times 10^{-3}$  and  $0.73 \times 10^{11}$  lines  $\text{cm}^{-2}$ , respectively, at the annealing temperature of 500 °C. Transmittance decreases with increasing temperature. It varies in the range of 65–85 % in visible and infrared regions. The optical band gap is found to vary in the range 2.4–2.85 eV for direct transitions. The best surface state is obtained at 400 °C. The RMS roughness was estimated to be 39.4–19.8 nm. Electrical measurements at room temperature show that the sheet

resistance decreases down to 130  $\Omega$  at 500 °C. The conductance and capacitance characterization at ambient temperature are also investigated and give interesting physical properties for photovoltaic applications.

## 1 Introduction

The interest for the indium sulfide thin films has increased during the last 10 years because of the high potential demonstrated by this material to be used as a buffer layer in  $\text{CuInS}_2$  based solar cells. Indium sulfide is a chalcogenide semiconductor with interesting properties for optoelectronics, and photovoltaic devices [1, 2].  $\text{In}_2\text{S}_3$  thin films appear to be promising candidates for many technological applications due to their stability and photoconductive behavior [3]. In addition, indium sulfide is promising as a buffer layer material for the solar cell replacing cadmium sulfide in order to avoid the toxicity of cadmium [4]. Indium sulfide is an n-type semiconductor with direct band gap energy in the range of 2–2.3 eV [5–7]. So far, indium sulfide films have been fabricated by various techniques such as spray pyrolysis [8, 9], ultrasonic dispersion [10], chemical bath deposition (CBD) [11], physical vapor deposition [12], hydrothermal [13], etc. Among these methods, spray pyrolysis is selected in this study because it allows preparing  $\text{In}_2\text{S}_3$  in large area thin films at low cost.

Only very few works have been reported to study the effect of tin doping on  $\text{In}_2\text{S}_3$  thin films, so as to modify their structural and electrical properties [14–16]. Moreover, a precise study on the properties of doped films is essential for the control of the doping parameters which are useful for electronic and optoelectronic applications.

Several post-deposition treatments are also used to improve the physical properties of the grown films.

✉ M. Kraini  
mabrouk.karini@gmail.com

<sup>1</sup> Laboratory of Physics of Materials and Nanomaterials Applied at Environment (LaPhyMNE), Faculty of Sciences of Gabes, Gabes University, 6072 Zrig, Tunisia

<sup>2</sup> Department of Physics, College of Sciences, Al Imam Mohammad Ibn Saud Islamic University (IMISU), Riyadh 11623, Saudi Arabia

<sup>3</sup> Faculté des Sciences, Unité de Recherches sur les Hétéro-Epitaxies et Applications (URHEA), 5000 Monastir, Tunisia

<sup>4</sup> Dep. de Física Aplicada, Universidad Politécnica de Cartagena (UPCT), Campus Alfonso XIII, 30203 Cartagena, Spain

<sup>5</sup> Laboratory of Magnetism and Nanotechnology, Institute of Technological Research, University of Santiago de Compostela, 15782 Santiago De Compostela, Spain

<sup>6</sup> Physics Department, College of Science, King Faisal University, P.O. Box 400, Hofuf 31982, Saudi Arabia

Usually, post-deposition annealing is used to improve structural, optoelectronic and electrical properties. Therefore, studies concerning the effects of annealing on the structural, optical and electrical properties of the films are very important in enhancing the devices efficiency.

The aim of this work is to investigate the effect of thermal annealing of  $\text{In}_2\text{S}_3\text{:Sn}$  films, grown on glass substrates by the spray pyrolysis technique, on their structural, optical and electrical properties.

## 2 Experiment

$\text{In}_2\text{S}_3$  films were deposited on glass substrates by the spray pyrolysis technique. These films were prepared by spraying an aqueous solution of indium chloride ( $\text{InCl}_3$ ) and thiourea ( $\text{CS}(\text{NH}_2)_2$ ) with a ratio of S:In = 2.5. The  $\text{InCl}_3$  concentration is  $10^{-2} \text{ mol l}^{-1}$ . Tin chloride ( $\text{SnCl}_4$ ) was used as a source of Sn with a molar ratio Sn/In = 1 %. The deposition conditions were optimized in order to obtain reproducible and good quality films. Compressed air was used as the carrier gas at a flow rate of  $6 \text{ l min}^{-1}$  and the flow rate of the solution during spraying was adjusted to be  $3 \text{ ml min}^{-1}$  and kept constant throughout the experiment. The nozzle-to-substrate distance was approximately 25 cm. The substrate temperature was maintained at  $350 \text{ }^\circ\text{C}$  within an accuracy of  $\pm 5 \text{ }^\circ\text{C}$ . When this temperature was reached, the solution was sprayed.

The films were then annealed for 2 h at 300, 400 and  $500 \text{ }^\circ\text{C}$  under nitrogen atmosphere. The thickness of the films is about  $0.28 \text{ }\mu\text{m}$ . These thicknesses were determined by double weight method. The detail of this method was reported elsewhere [17]. These thickness values were also confirmed by scanning electron microscopy measurement calibration. The crystalline structure of the films was analyzed by X-ray diffraction (XRD) using  $\text{Cu-K}\alpha$  radiation ( $1.5406 \text{ \AA}$ ) of a Bruker D8 Advance diffractometer operating at 40 kV, 40 mA. Their chemical composition was studied with the help of Energy Dispersive Spectroscopy (EDS). The surface morphology was investigated by means of scanning electron microscopy (SEM) using a Zeiss FE-SEM Ultra PLUS microscope equipped with electron dispersive X-ray spectroscopy (EDS) for microanalysis detection, and atomic force microscopy using XE-100 instrument (Park Systems Corporation) in non-contact mode (NC-AFM). The optical properties were analyzed with a Shimadzu UV 3101 PC spectrophotometer, in a wavelength range from 300 to 2400 nm. Sheet resistance was examined by a Four-point probe. For ac measurements, an Agilent 4294A impedance analyzer was used to collect impedance measurements over a wide frequency range (40 Hz–20 MHz).

## 3 Results and discussion

### 3.1 Structure

Figure 1 shows the XRD patterns of  $\text{In}_2\text{S}_3\text{:Sn}$  films annealed at temperatures of 300, 400 and  $500 \text{ }^\circ\text{C}$ , for 2 h. The films pattern indicates that all the peaks correspond to the cubic structure of polycrystalline  $\text{In}_2\text{S}_3$  with diffractions from (111), (220), (311), (400), (222), (511), (440) and (444) planes, according to JCPDS card No. 32-0456. However, the XRD pattern of the thin film annealed at  $500 \text{ }^\circ\text{C}$  shows also the presence of  $\text{In}_2\text{O}_3\text{:Sn}$  (ITO) secondary phase, according to the JCPDS card No. 88-0773. The formation of ITO films is due to the evaporation of sulfur atoms during the thermal annealing process and the occupation of the sulfur sites by oxygen atoms. Besides, with an increase of annealing temperature, the intensity of the (311) peak increases indicating an improvement in the texture of the layers. In addition, it is found that its FWHM decreases from  $0.32^\circ$  for as-deposited films to  $0.22^\circ$  for annealing temperature of  $500 \text{ }^\circ\text{C}$ . Thus the results indicate that the crystalline quality is enhanced as the annealing temperature is increased.

The inter-reticular distance  $d_{311}$  calculated from XRD results (Table 1) varies from 3.238 to  $3.250 \text{ \AA}$  with the annealing temperature. The  $d_{311}$  value coincides well with that of the  $\text{CuInS}_2$  ternary compound, which is equal to  $d_{112} = 3.1957 \text{ \AA}$  (JCPDS card No. 27-0159). This may imply that the growth of the  $\text{In}_2\text{S}_3$  thin films according to the (311) direction, are advantageous for the  $\beta\text{-In}_2\text{S}_3(\text{n})/\text{CuInS}_2(\text{p})$  thin film photovoltaic devices, since it will assure a lattice match with a minimum of misorientation and low structural defect densities at the interface of the junction.

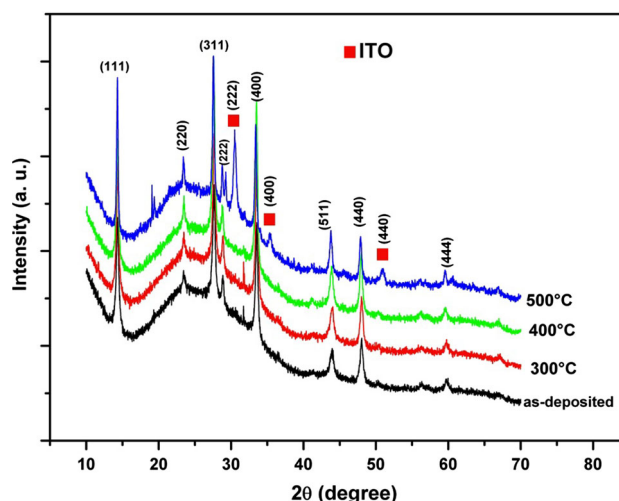


**Fig. 1** XRD patterns of  $\text{In}_2\text{S}_3\text{:Sn}$  films as a function of the annealing temperature

**Table 1** Position of (311) peak and some relevant parameters

Annealing temperature (°C)	2θ (°)	B (°)	d <sub>311</sub> (Å)	D (nm)	δ (10 <sup>11</sup> lines cm <sup>-2</sup> )	ε (10 <sup>-3</sup> )
As-deposited	27.626	0.32	3.241	26.14	1.46	1.23
300	27.626	0.27	3.238	30.12	1.10	0.30
400	27.620	0.26	3.250	31.60	1.00	4.01
500	27.546	0.22	3.247	37	0.73	3.08

The microstrain ( $\epsilon$ ), defined as a measure of the change in a body size or shape, referred to its original size or shape, developed in the films could be indirectly measured from the change of the lattice spacing. Indeed, the microstrain generally induces a change in the position of diffraction peaks. The strain ( $\epsilon$ ) was assessed using the relation [18]:

$$\epsilon = \frac{d^{hkl} - d_0^{hkl}}{d_0^{hkl}} \quad (1)$$

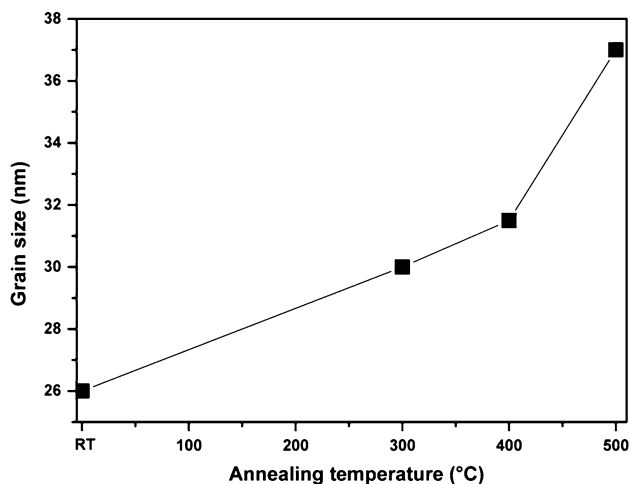
where  $d^{hkl}$  is the lattice spacing obtained from the Bragg angle  $\theta^{hkl}$ , and  $d_0^{hkl}$  ( $d_0^{hkl} = 3.237$  Å; JCPDS card No. 32-0456) is the strain-free lattice spacing of the (hkl) lattice planes.

The variation of the microstrain ( $\epsilon$ ) as a function of annealing temperature is reported in Table 1. The result shows that the strain in the films is tensile ( $\epsilon > 0$ ) for different annealing temperature [19].

The grain size (D) of In<sub>2</sub>S<sub>3</sub>:Sn samples was determined by using the FWHM of the (311) main peak [20]:

$$D^2 = \left[ \frac{0.9\lambda}{B \cos \theta} \right]^2 + [4\epsilon \tan \theta]^2 \quad (2)$$

where B is the full width at half maximum in radians,  $\lambda$  is the wavelength of X-ray,  $\theta$  is the Bragg angle.

**Fig. 2** Grain size of In<sub>2</sub>S<sub>3</sub>:Sn films as a function of the annealing temperature

The calculated sample grain sizes are shown in Table 1. Figure 2 reveals an increase of the grain size from 26.14 to 37 nm with annealing temperature. This is mainly due to the coalescence of smaller nuclei or neighboring grains resulting in the improvement of crystallinity [17, 21].

The dislocation density ( $\delta$ ) is described as the length of dislocation lines per unit volume of the crystal [22]. The dislocation density gives information about the crystal structure. The dislocation density for preferential orientation (311) can be calculated using the formula [23]:

$$\delta = \frac{1}{D^2} \quad (3)$$

The study of the variation of the dislocation density of In<sub>2</sub>S<sub>3</sub>:Sn (Table 1) reveals that it decreases with annealing temperature from  $1.46 \times 10^{11}$  to  $0.73 \times 10^{11}$  lines cm<sup>-2</sup>. This behavior can be explained by the change of the grains size (D) with annealing temperature. Indeed, the smaller crystallites have a greater surface to volume ratio, thus giving rise to the dislocation network [24]. The above results show that the lowest values of the residual microstrain and the dislocation density are obtained for annealing temperature of about 500 °C, for which the crystallinity of the In<sub>2</sub>S<sub>3</sub>:Sn thin films is the best one.

### 3.2 Microanalysis

The film composition has also been investigated by means of EDS. Atomic percentage of the elements in the films is reported in Table 2. These values are an average value obtained from measurements at least in four different regions of each film. As expected, the Sn percentage remains constant for all the annealing temperatures. Thus, the small amount of oxygen detected at temperatures lower than 500 °C could be originated from the glass substrate.

**Table 2** Chemical compositions of In<sub>2</sub>S<sub>3</sub>:Sn thin films annealed at different temperatures using EDS

Elements	As-deposited	300 °C	400 °C	500 °C
S (at.%)	32.93	28.47	23.83	9.60
In (at.%)	18.12	16.43	15.28	15.85
Sn (at.%)	13.06	14.50	13.87	13.85
O (at.%)	35.89	40.60	47.02	60.70

Indeed, for our samples having small thin film thicknesses of about 280 nm, glass substrate is also probed.

It can also be seen that O content increases at 500 °C whereas sulfur content in the film decreases. This is probably due to the re-evaporation of sulfur from the film during the post-deposition annealing because of its high vapor pressure, forming S vacancies. These defects were filled by oxygen atoms by diffusion from surface into the bulk of the films. The high percentage of O content (60 %) combined with the low content of S (9.6 %) at annealing temperature of 500 °C confirms the presence of ITO phase as revealed by the results of XRD results in Fig. 1.

### 3.3 Morphology

Figure 3 exhibits the scanning electron micrographs of the samples. As seen, the surface morphology of the films depends on the annealing temperature. The micrographs show that the nanostructure of the condensed films has a particle growth type. However, the films had nearly circular shaped grains that were uniformly distributed over the substrate surface. It is also observed that the film became denser with densely packed grains with the increase of annealing temperature due to the coalescence phenomenon. It is also seen that the samples are free of pinholes and cracks.

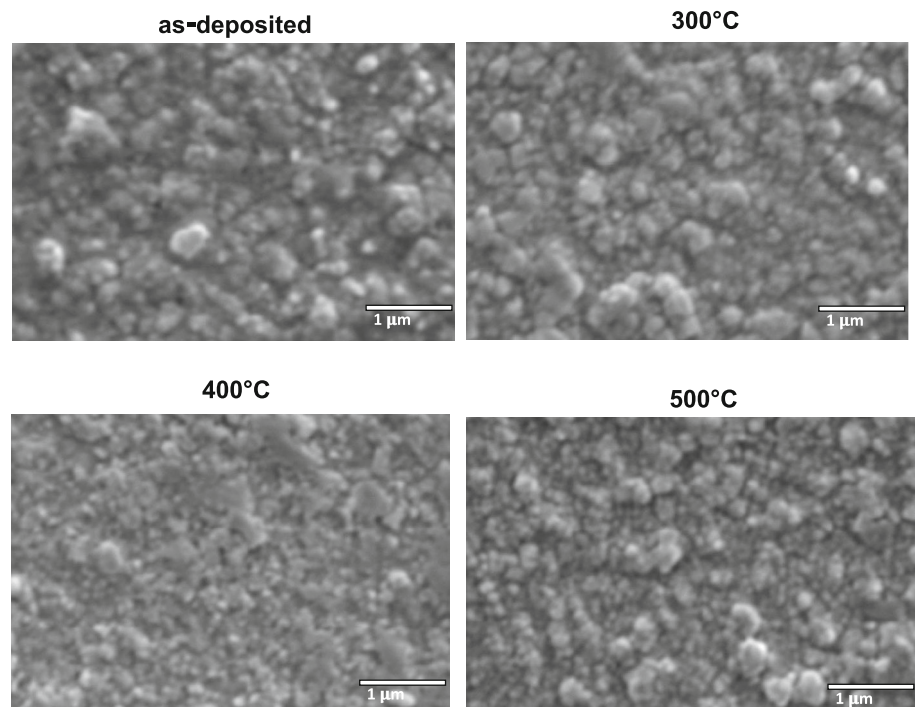
The surface morphology of the layers was also studied by NC-AFM technique. Figure 4 shows 3D-NC-AFM images ( $2\ \mu\text{m} \times 2\ \mu\text{m}$ ) and peak-to-valley ( $R_{pv}$ ) size distribution of  $\text{In}_2\text{S}_3:\text{Sn}$  films annealed at different temperatures.

These images show that the surface morphologies of the films are dependent on the annealing temperature. They reveal that the substrate is entirely covered with grains of different sizes and the grain sizes along the surface of the deposited films increase with increasing annealed temperature. When the temperature increases from room temperature to 500 °C, the average particle size shows good agreement with the XRD results in increasing from 24.6 to 37.7 nm, respectively. This behavior can be attributed to the nucleation and island formation on the films surface as  $\text{In}_2\text{S}_3:\text{Sn}$  grains are growing. It can be observed that the films are continuous and rather smooth. The RMS roughness was estimated to be in the range 39.4–19.8 nm. The RMS roughness values decreased with increasing annealing temperature. This behaviour can be due to the fact that with increasing the annealing temperature, the grain size increases and surface morphology becomes uniform and more compact. Thus, we observed a reduction of the roughness and improvement of the surface smoothness with increasing annealing temperature. This feature would be well for forming abrupt junctions in p–n device structures such as solar cells.

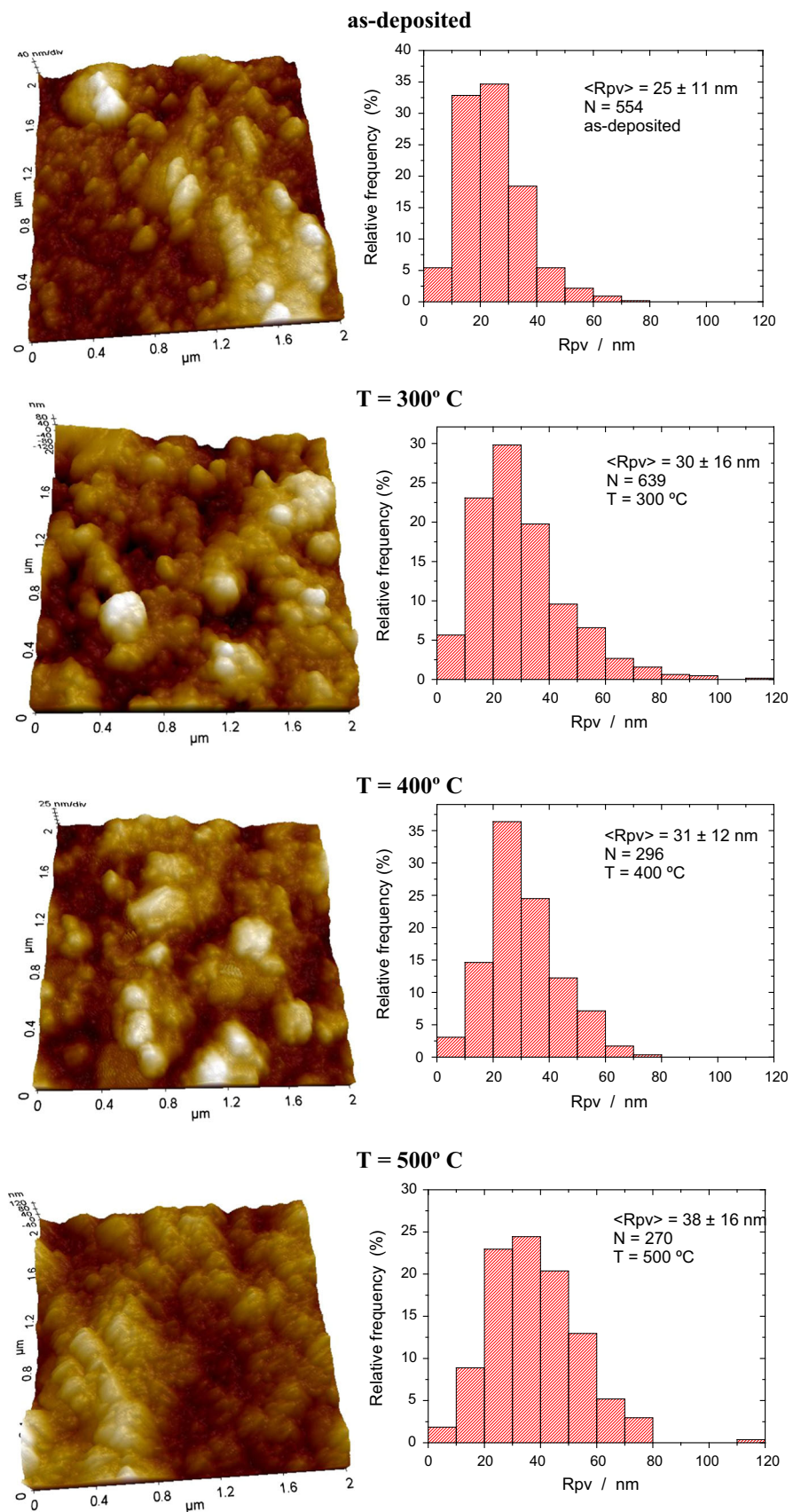
### 3.4 Optical analysis

The evolution of transmission spectra measurement in the wavelength range 300–2400 nm (Fig. 5) is also depicted in order to investigate the effect of annealing temperature on the optical performances of the  $\text{In}_2\text{S}_3:\text{Sn}$  thin films that can

**Fig. 3** SEM images of  $\text{In}_2\text{S}_3:\text{Sn}$  thin films annealed at different temperatures



**Fig. 4** NC-AFM images and peak-to-valley ( $R_{pv}$ ) size distributions of as-prepared and annealed  $\text{In}_2\text{S}_3:\text{Sn}$  thin films



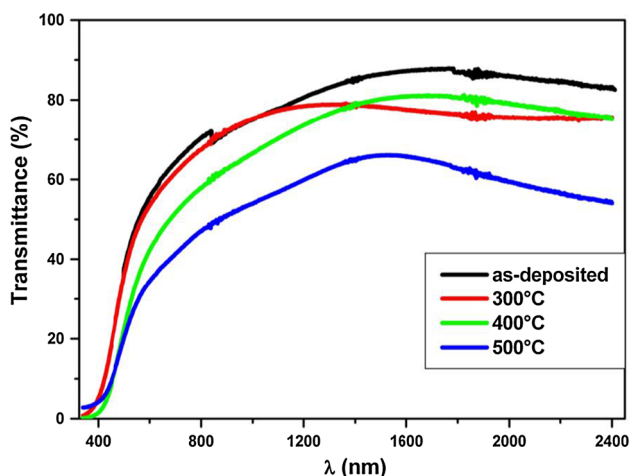


**Fig. 5** Transmittance spectra of  $\text{In}_2\text{S}_3:\text{Sn}$  films as a function of the annealing temperature

be used as a buffer layers. The high transmittance indicates a fairly smooth surface and a relatively good homogeneity of the film. One can see from the transmittance value that the UV radiations are completely absorbed. Therefore, we can deduce that these films may be used as UV detector. The transmittance decreases after the annealing and there is a shift of the peaks towards shorter wavelengths. This phenomenon is due to the increase in the density of free charge carriers after annealing which results in more absorption of light [25]. Generally, several parameters influence the optical transmittance [26, 27].

The dependence of the absorption coefficient on photon energy in the high absorption regions is carried out to obtain the detailed information about the band gap energy. The optical band gap of the films is determined by the following relation [28]:

$$\alpha h\nu = A(h\nu - E_g)^n \tag{4}$$

where  $A$  is a constant,  $h$  is the Planck constant,  $\nu$  is the frequency,  $E_g$  is the optical band gap and the exponent  $n$  characterizes the nature of band transition. Indeed,  $n = 1/2$  and  $2$  corresponds to direct allowed and indirect forbidden transitions, respectively. Figure 6 shows the variation of  $(\alpha h\nu)^2$  against  $h\nu$ . The band gap energy is determined by extrapolating the straight line portion to the energy basis at  $\alpha = 0$ . We observed that the curve has a very good straight line fit from 2.4 to 2.85 eV. This result indicates that the optical energy gap is a direct transition.

The Urbach energy tailing which characterizes the optical properties changes, especially the optical absorption in the material, follows the empirical Urbach law [29, 30]:

$$\alpha = \alpha_0 \exp\left(\frac{h\nu}{E_U}\right) \tag{5}$$

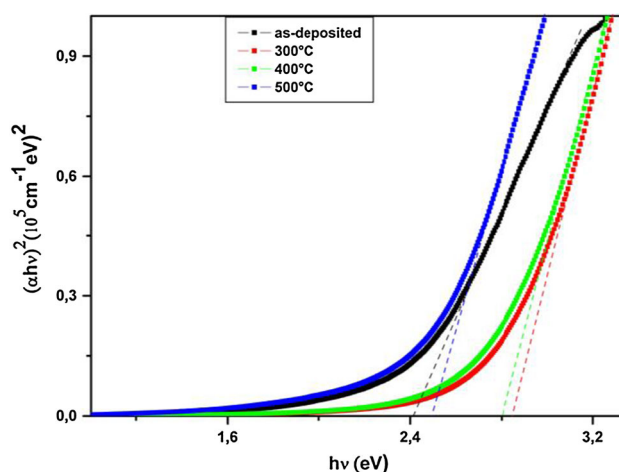


**Fig. 6** Variation of  $(\alpha h\nu)^2$  versus photon energy of  $\text{In}_2\text{S}_3:\text{Sn}$  films as a function of the annealing temperature

$$E_U = \left[ \frac{d \ln \alpha}{dh\nu} \right]^{-1} \tag{6}$$

where  $\alpha_0$  is a constant,  $E_U$  is the Urbach energy, which characterizes the slope of the exponential limit (Fig. 7).  $E_U$  values are calculated from the inverse of the slope of  $\ln \alpha$  versus  $h\nu$  [31]. The calculated values of the optical band gap energy  $E_g$  and  $E_U$  of  $\text{In}_2\text{S}_3:\text{Sn}$  thin films as a function of annealing temperature are shown in Fig. 8. Generally in polycrystalline semiconductors, the energy band gap can be affected by several parameters [32–34]. It is observed that annealing temperature greatly affects the optical band gap of the film. The systematic change of  $E_g$  with annealing

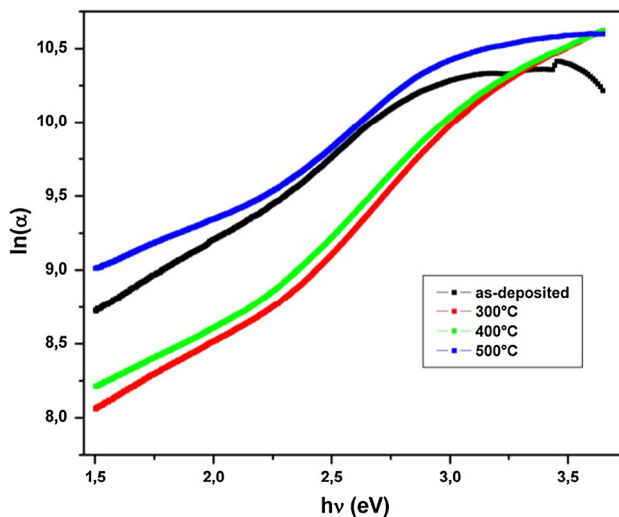


**Fig. 7** Variation of  $\ln \alpha$  versus photon energy of  $\text{In}_2\text{S}_3:\text{Sn}$  films as a function of the annealing temperature

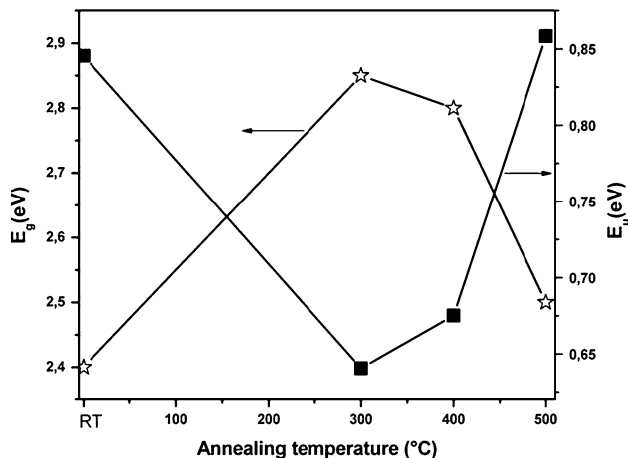


**Fig. 8** Band gap energy and Urbach energy of  $\text{In}_2\text{S}_3:\text{Sn}$  films as a function of the annealing temperature

temperature suggests the substitution of the sulfur by oxygen in the lattice, also by interstitial In atoms or oxygen vacancies. This increase in band gap can be attributed to the incorporation of oxygen as sulfur concentration in films decreases. From EDS (Table 2), it is clear that sulfur concentration decreases for annealing temperatures between 300 and 500 °C. Barreau et al. [35] reported an increase in band gap with oxygen concentration. But it could be seen that, with an increase of the oxygen concentration above an optimum value, the band gap decreased. The sharp decrease of energy band gap at higher annealing temperature (500 °C) could be due to the formation of localized states in the band gap region. These states might be induced in the band gap because of the structural disorder due to the sulfur deficiency. This high concentration of impurity states cause the band structures to be perturbed, resulting in a prolonged tail extending into the energy band gap. This result is consistent with the results of the XRD analysis. The Urbach tail was evaluated to quantify the structural disorder. The evaluated Urbach tail width increases from 0.64 to 0.85 eV with the increase in annealing temperature up to 500 °C. Moreover, the energy band gap could also be influenced by the variation of particle size with annealing temperature as it is in the nanometer range, though it is not close to the Bohr radius. Therefore in the present study, the improvement in the particle size could contribute to the decrease of energy band gap of the films with the increase of annealing temperature [36]. A similar behavior for energy band gap variation was observed by Revathi et al. [21].

### 3.5 Electrical characterization

All the films exhibited an n-type conductivity, which means that the annealing did not change the type of the

majority carriers. Moreover, as seen in Table 3, the decrease in the sheet resistance of the sample down to 130  $\Omega$  after annealing at 500 °C is consistent with the results of the XRD diffractograms. Indeed, the increase of grain size after annealing results in smaller effect of grain boundary resistance and then lower resistivity of the films. Generally, the electrical conductivity of a semiconductor depends on the thermal excitation of electron, impurities and lattice defects such as dislocation, stacking faults [37]. The annealing temperature controls the resistivity of the material and adapts it to device applications [38]. The resistivity decrease is proved to be quite advantageous for photovoltaic applications.

### 3.6 Conductance and capacitance-frequency characteristics

In order to characterize the electrical properties, a 2 mm diameter aluminum contact is deposited by vacuum evaporation technique at pressure  $\sim 5 \times 10^{-6}$  Torr for all samples.

The ac electrical conductivity of the  $\text{In}_2\text{S}_3:\text{Sn}$  films for different annealing temperatures has been studied in the frequency range 40 Hz–20 MHz and ambient temperature. The frequency dependence of the measured conductivity is shown in Fig. 9a. Ac conductance spectra exhibit two behaviors for all temperatures. First, at low frequencies, we can observe for these samples a rise in the conductance value with annealing temperature. The conductance patterns show a frequency independent plateau in the low frequency region.

Second, at high frequency part, the conductance  $G$  proves the existence of a hopping mechanism. The frequency at which a change in the slope of the conductance spectrum occurs is conventionally known as the “hopping frequency”. This behavior obeys the universal power law. The origin of the frequency-dependence of conductance lies in the relaxation phenomena arising due to mobile charge carriers [39]. When a mobile charge carrier hops to a new site from its original position, it remains in a state of displacement between two potential well energy minima.

As mentioned above, the conduction behavior of the material obeys the power law [40]:

$$G(\omega, T) = G_{dc}(T) + A(T)\omega^{s(\omega, T)} \quad (7)$$

where  $G_{dc}$  is the dc conductance (frequency independent plateau in the low frequency region),  $A$  is a constant dependent on the temperature and  $s$  is the fractional exponent between 0 and 1, corresponding to a hopping process. This parameter is frequency independent but temperature and material dependent. The exponent  $s$  can be extracted from the slope of straight-line, fitting the experimental data at different frequency regions. The small value of ( $s < 1$ )

**Table 3** Sheet resistance and RMS roughness of  $\text{In}_2\text{S}_3:\text{Sn}$  films as a function of the annealing temperature

Annealing temperature ( $^{\circ}\text{C}$ )	As-deposited	300 $^{\circ}\text{C}$	400 $^{\circ}\text{C}$	500 $^{\circ}\text{C}$
Sheet resistance ( $\Omega \text{ sq}^{-1}$ )	$18.4 \times 10^9$	$1.3 \times 10^9$	$37.4 \times 10^3$	130
RMS roughness (nm)	39.4	30	25.7	19.8

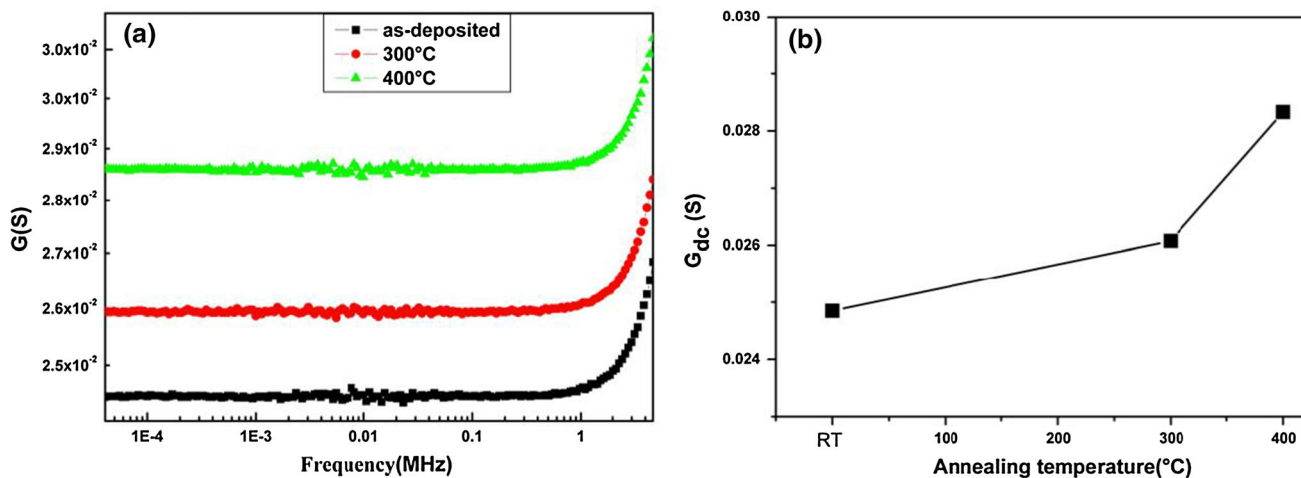


**Fig. 9** The conductance versus frequency of annealed  $\text{In}_2\text{S}_3:\text{Sn}$  films at room temperature (a) and  $G_{dc}$  as function annealing temperature (b)

suggests involving a translational motion with a sudden hopping [41, 42]. The  $G_{dc}$  is improved by annealing temperature (Fig. 9b). The frequency dependence of the conductance is governed by hopping conductivity [43].

The capacitance versus frequency at different annealing temperatures is plotted in Fig. 10. The capacity is very low and independent both to the frequency and annealing temperature, indicating that the contact Al/ $\text{In}_2\text{S}_3:\text{Sn}$  is ohmic. The capacitance response for these samples shows that the capacitance behavior is typical of material with traps [44]. It is clearly seen that the measured capacitances decrease with the increase in frequency. A high value of

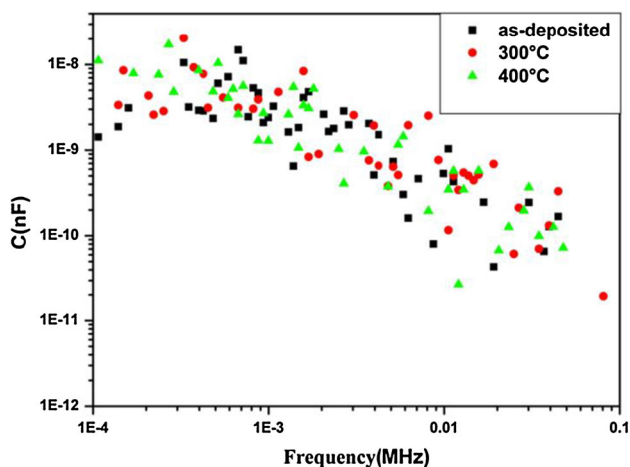


**Fig. 10** The capacitance versus frequency of annealed  $\text{In}_2\text{S}_3:\text{Sn}$  films at room temperature

capacitance at low frequencies is due to the excess of capacitance resulting from the interface states that can follow the ac signal [45]. With the increasing of frequency, the capacitance decreases.

### 4 Conclusion

Tin doped indium sulfide thin films were elaborated with spray technique for  $\text{Sn}/\text{In} = 1\%$  molar ratio. These films annealed at different temperatures were polycrystalline with cubic structure. The residual microstrain and dislocation network seems to be reduced respectively to the values  $3.08 \times 10^{-3}$  and  $0.73 \times 10^{11}$  lines  $\text{cm}^{-2}$  for an annealing temperature of about 500  $^{\circ}\text{C}$ , for which the crystallinity of the  $\text{In}_2\text{S}_3:\text{Sn}$  thin films is the best. This film presents an ITO secondary phase. The investigation of optical properties reveals that the films exhibit an increase of the band gap with the annealing temperature. Band gap of  $\text{In}_2\text{S}_3:\text{Sn}$  could be varied from 2.4 to 2.85 eV. The scanning electron micrographs show that the samples are free of pinholes and cracks. The coalescence of grains is improved with annealing temperature. The RMS roughness was estimated to be 39.4–19.8 nm. Electrical measurements show that, at low frequency, the conductance is independent of frequency and improved by annealing temperature. At high frequency, the conductance is governed by hopping process. Wide band gap and low resistive  $\text{In}_2\text{S}_3:\text{Sn}$  films could be obtained which are highly useful for photovoltaic applications.



**Acknowledgments** This work was supported by the funding of different organizations: MINECO, Spain (project MAT2012-36754-C02-01); and Xunta de Galicia, Spain (Grupos Ref. Comp. GRC2013-044, FEDER Funds).

## References

1. R. Naik, S.K. Parida, C. Kumar, R. Ganesan, K.S. Sangunni, J. Alloy. Compd. **522**, 172–177 (2012)
2. K. Hara, K. Sayama, H. Arakawa, Sol. Energy Mater. Sol. Cells **62**, 441–447 (2000)
3. L. Bhira, H. Essaidi, S. Belgacem, G. Couturier, J. Salardenne, N. Barreau, J.C. Bernede, Phys. Status Solidi A **181**, 427–435 (2000)
4. A.S. Cherian, M. Mathew, C.S. Kartha, K.P. Vijayakumar, Thin Solid Films **518**, 1779–1783 (2010)
5. P.M. Sirimanne, S. Shiozaki, N. Sonoyama, T. Sakata, Sol. Energy Mater. Sol. Cells **62**, 247–258 (2000)
6. N. Bouguila, A. Timoumi, H. Bouzouita, E. Lacaze, H. Bouchriha, B. Rezig, Eur. Phys. J. Appl. Phys. **63**, 20301 (2013)
7. J. Herrero, J. Ortega, Sol. Energy Mater. **17**, 357–368 (1988)
8. T.T. John, M. Mathew, C.S. Kartha, K.P. Vijayakumar, T. Abe, Y. Kashiwaba, Sol. Energy Mater. Sol. Cells **89**, 27–36 (2005)
9. M. Mathew, R. Jayakrishnan, P.M. Ratheesh Kumar, C. Sudha Kartha, K.P. Vijayakumar, J. Appl. Phys. **100**, 033504 (2006)
10. Z. Li, X. Tao, Z. Wu, P. Zhang, Z. Zhang, Ultrason. Sonochem. **16**, 221–224 (2009)
11. B. Asenjo, C. Sanz, C. Guillén, A.M. Chaparro, M.T. Gutiérrez, J. Herrero, Thin Solid Films **515**, 6041–6044 (2007)
12. N. Barreau, J.C. Bernède, C. Deudon, L. Brohan, S. Marsillac, J. Cryst. Growth **241**, 4–14 (2002)
13. P.G.S. Abadi, M.S. Niasari, F. Davar, Superlattice Microstruct. **53**, 76–88 (2013)
14. R.S. Becker, T. Zheng, J. Elton, M. Saeki, Sol. Energy Mater. **13**, 97–107 (1986)
15. M. Mathew, M. Gopinath, C. Sudha Kartha, K.P. Vijayakumar, Y. Kashiwaba, T. Abe, Sol. Energy **84**, 888–897 (2010)
16. M. Kilani, C. Guasch, M. Castagne, N.K. Turki, J. Mater. Sci. **47**, 3198–3203 (2012)
17. M. Kraini, N. Bouguila, I. Halidou, A. Timoumi, S. Alaya, Mater. Sci. Semicond. Process. **16**, 1388–1396 (2013)
18. U. Welzel, J. Ligot, P. Lamparter, A.C. Vermeulen, E.J. Mittemeijer, J. Appl. Cryst. **38**, 1–29 (2005)
19. B. Yahmadi, N. Kamoun, C. Guasch, R. Bennaceur, Mater. Chem. Phys. **127**, 239–247 (2011)
20. G. Will, *Powder Diffraction* (Springer, Berlin, 2006)
21. N. Revathi, P. Prathap, R.W. Miles, K.T. Ramakrishna, Reddy. Sol. Energy Mater. Sol. Cells **94**, 1487–1491 (2010)
22. K. Ravichandran, P. Philominathan, Sol. Energy **82**, 1062–1066 (2008)
23. V. Bilgin, S. Kose, F. Atay, I. Akyuz, Mater. Chem. Phys. **94**, 103–108 (2005)
24. P. Roy, S.K. Srivastava, Thin Solid Films **496**, 293–298 (2006)
25. S.J. Ikhmayies, R.N. Ahmad-Bitar, Appl. Surf. Sci. **255**, 2627–2631 (2008)
26. A. Larena, F. Millan, G. Perez, G. Pinto, Appl. Surf. Sci. **187**, 339–346 (2002)
27. M. Öztas, M. Bedir, Thin Solid Films **516**, 1703–1709 (2008)
28. N. Pentyala, R.K. Guduru, E.M. Shnerpunas, P.S. Mohanty, Appl. Surf. Sci. **257**, 6850–6857 (2011)
29. F. Urbach, Phys. Rev. **92**, 1324 (1953)
30. S. Ilican, Y. Caglar, M. Caglar, J. Optoelectron. Adv. M. **10**, 2578–2583 (2008)
31. S. Ilican, Y. Caglar, M. Caglar, M. Kundakci, A. Ates, Int. J. Hydrogen Energy **12**, 5201–5207 (2009)
32. C.D. Lokhande, A.U. Ubale, P.S. Patil, Thin Solid Films **302**, 1–4 (1997)
33. R.S. Mane, C.D. Lokhande, Mater. Chem. Phys. **82**, 347–354 (2003)
34. J.D. Dow, D. Redfield, Phys. Rev. B **5**, 594 (1972)
35. N. Barreau, S. Marsillac, D. Albertini, J.C. Bernede, Thin Solid Films **403–404**, 331–334 (2002)
36. J. El Ghoul, C. Barthou, L. El Mir, Phys. E. **44**, 1910–1915 (2012)
37. F. Rahman, J. Podder, Surf. Rev. Lett. **20**, 1350014 (2013)
38. M. Nisha, S. Anusha, A. Antony, R. Manoj, M.K. Jayaraj, Appl. Surf. Sci. **252**, 1430–1435 (2005)
39. H. Li, X. Guo, Curr. Appl. Phys. **13**, 500–504 (2013)
40. I. Najeh, N. Ben Mansour, M. Mbarki, A. Houas, J.P. Nogier, L. El Mir, Solid State Sci. **11**, 1747–1751 (2009)
41. H. Nefzi, F. Sediri, H. Hamzaoui, N. Gharbi, J. Solid State Chem. **190**, 150–165 (2012)
42. S. Sen, R.N.P. Choudhary, Mater. Chem. Phys. **87**, 256–263 (2004)
43. K.K. Patanakar, S.A. Patil, K.V. Sivakumar, R.P. Mahajan, Y.D. Kolekar, M.B. Kothale, Mater. Chem. Phys. **65**, 97–102 (2001)
44. D.M. Taylor, H.L. Gomez, J. Phys. D Appl. Phys. **28**, 2554–2568 (1995)
45. A.F. Özdemir, A. Gök, A. Türüt, Thin Solid Films **425**, 210–215 (2007)